

# Where's the Doughnut? LBV bubbles and Aspherical Fast Winds<sup>8</sup>

Adam Frank <sup>1,5</sup>, Dongsu Ryu <sup>2,3,6</sup>, and Kris Davidson <sup>4,7</sup>

Received \_\_\_\_\_; accepted \_\_\_\_\_

---

<sup>1</sup>Dept. of Physics and Astronomy, Bausch and Lomb Building, Univ. of Rochester, Rochester, NY 14627-0171

<sup>2</sup>Department of Astronomy, University of Washington, Box 351580, Seattle, WA 98195-1580

<sup>3</sup>Department of Astronomy & Space Science, Chungnam National University, Daejeon 305-764, Korea

<sup>4</sup>Department of Astronomy, University of Minnesota, Minneapolis, MN 55455

<sup>5</sup>email: afrank@alethea.pas.rochester.edu

<sup>6</sup>email: ryu@hermes.astro.washington.edu

<sup>7</sup>email: kd@ast1.spa.umn.edu

<sup>8</sup>Submitted to the Astrophysical Journal

## ABSTRACT

In this paper we address the issue of the origin of LBV bipolar bubbles. Previous studies have explained the shapes of LBV nebulae, such as  $\eta$  Car, by invoking the interaction of an isotropic fast wind with a previously deposited, slow aspherical wind (a “slow torus”). In this paper we focus on the opposite scenario where an *aspherical fast wind* expands into a previously deposited *isotropic slow wind*. Using high resolution hydrodynamic simulations, which include the effects of radiative cooling, we have completed a series of numerical experiments to test if and how aspherical fast winds effect wind blown bubble morphologies. Our experiments explore a variety of models for the latitudinal variations of fast wind flow parameters. The simulations demonstrate that aspherical fast winds can produce strongly bipolar outflows. In addition the properties of outflows recover some important aspects of LBV bubbles which the previous ”slow torus” models can not.

*Subject headings:* hydrodynamics - stars: mass loss - stars: supergiants

## 1. Introduction

In just a few years the HST has transformed our understanding of the massive unstable stars know as Luminous Blue Variables (LBVs). Recent observations have revealed a number of LBVs or LBV candidates to be surrounded by extended *aspherical* outflows. The most extraordinary of these is the markedly bipolar nebula surrounding  $\eta$  Carinae (“the homunculus”: Hester *et al.* 1991; Ebbets *et al.* 1993; Humphreys & Davidson 1994). Other LBVs show nebulae with varying degrees of asphericity from elliptical (R127: Nota *et al.* 1995) to strongly bipolar (which we define though the presence of an equatorial waist: HR Carinae: Nota *et al.* 1995; Weis *et al.* 1996).

These morphologies are quite similar to what has been observed in Planetary Nebulae (PNe) which arise from low mass stars (Balick 1987; Manchado *et al.* 1996). The aspherical shapes of PNe have been successfully explained through a scenario termed the “Generalized Interacting Stellar Winds” model (GISW: Kwok, Purton & Fitzgerald 1978, Kwok 1982, Kahn 1983, Frank *et al.* 1993; Frank & Mellema 1994; Mellema & Frank 1995). In the GISW model an isotropic fast wind from the central star (a proto-white dwarf) expands into an aspherical (toroidal) slow wind ejected by the star in its previous incarnation as a Asymptotic Red Giant. High densities in the equatorial plane constrain the expansion of the fast wind. The expanding shock which forms quickly assumes an elliptical prolate geometry. If the ratio of mass density between the equator and pole (a parameter we call  $q$ ,  $q = \rho_e/\rho_p$ ) is high enough, then the elliptical bubble eventually develops a waist and becomes bipolar.

The similarity of PNe and LBV nebulae has led to the suggestion that both families of objects are shaped in similar ways. In Frank, Balick, & Davidson 1995 (hereafter: FBD) a GISW model for  $\eta$  Car was presented in which a spherical “outburst” wind expelled during the 1840 outburst expanded into a toroidal “pre-outburst” wind. FBD showed that the resulting bipolar outflow could recover both the gross morphology and kinematics of the Homunculus. Nota *et al.* 1995 (hereafter NLCS) used a similar model for other LBV nebulae presenting a unified picture of the development of LBV outflows. More recently Garcia-segura *et al.* 1997 (hereafter GLM) presented a model which also relied on the GISW scenario but which changed the order of importance of

the winds. The novel aspect of GLM’s study was to include the effects of stellar rotation. Using the Wind Compressed Disk model of Bjorkman & Cassinelli 1992, GLM showed that a strong equator to pole density contrast would likely form *during the outburst* when the star is close to the Eddington limit and rotation can deflect wind streamlines toward the equator. In their model it is the “post-outburst” mass loss (which was not considered in either FBD or NLCS) that acts as the fast wind. The post-outburst wind in GLM’s model “inflates” the bipolar bubble via its interaction with the toroidal outburst wind.

All these models have demonstrated the potential efficacy of the GISW scenario by recovering the basic shapes observed in LBV nebulae. However, by relying on the presence of a slow torus they are troubling in their mutual inconsistency. Specifically the question “Where is the torus?” must be answered. Does the torus form during the outburst phase as in GLM or does it form in the pre-outburst wind as in FBD and NLCS? Without invoking binary interactions or a pre-existing disk left over from the stellar formation process, it may be difficult to get a strong toroidal density contrast in the pre-outburst environment.

Stepping back further one can also ask if a disk is needed at all? The latter question arises from consideration of new HST images of  $\eta$  Car (Morse *et al.* 1997) which reveal the disk to be so highly fragmented that it may be more reasonable to consider the structure to be a “skirt” of individual clumps of ejecta rather than a continuous feature. This point is crucial since a discontinuous equatorial spray of isolated bullets can not hydrodynamically constrain an isotropic stellar wind to form a bipolar outflow. Thus we are led to consider an alternative model to the one proposed by FBD, NLCS and GLM which further generalizes the GISW model by turning that scenario on its head. In what follows we consider the case of an *aspherical fast wind* interacting with an *isotropic slow wind*. We imagine a fast wind ejected with higher velocity along the poles than along the equator. The question we wish to answer is can such a wind, expanding into an isotropic environment, account for the shapes of LBV nebulae.

There are a number of reasons for pursuing this line of investigation some of which were cited above as criticisms of the “classic” GISW model. More importantly, however, theoretical models

admit the possibility of aspherical fast winds in massive stars. Pauldrach & Puls 1990 have shown that a discontinuity (bistability) in mass loss and velocity occurs when the effective gravity of the star drops below a critical value. Lamers & Pauldrach 1991 used these results to demonstrate that stellar rotation can induce latitudinal changes in  $g_{eff}$  and the optical depth of the wind. The change in optical depth puts the polar and equatorial regions of the star on different sides of the bistability limit. A high velocity, low density wind forms at the poles, and low velocity, high density wind forms along the equator. It should be noted that the Wind Compressed Disk (WCD) model of Bjorkman & Cassinelli 1992 also produces aspherical winds since the equatorial focusing occurs close to the star. Thus a wind that has been shaped by the WCD mechanism, if it is expanding into a slower moving environment, should be considered an aspherical fast wind, *i.e.* the issue is always the velocity (and density) of previously ejected material. It is worth noting however that recent numerical models of the WCD mechanism (Owocki, Cranmer & Gayley 1996) which include non-radial line forces found inhibition of the wind compression and mass loss in the equator. Instead a net flow in the pole-ward direction was formed. This is, therefore, yet another way by which fast winds might become aspherical. Finally, and most importantly, there is direct evidence for asphericity in fast winds. Observations of the wind of AG Carinae (Leitherer *et al.* 1994) imply a pattern of densities and velocities from pole to equator much like that described in Lamers & Pauldrach 1991. Finally we note that it is worthwhile to pursue this kind of investigation simply because it has not been done before. The GISW model and its variations has been very successful in accounting for a variety of bipolar outflow phenomena (Mellema, Eulderink & Icke 1991; Blondin & Lundqvist 1993; Frank, Balick & Livio 1996). Since the effect of aspherical fast winds has yet to be investigated the potential of finding useful results is high which argues for a detailed study.

We note that this paper represents an initial exploratory study. We are using an admittedly ad-hoc formalism to control the asphericity of the fast wind and we have not tuned our parameters to the accepted values for any particular LBV. Our purpose in this paper is to map out the broad consequences of including aspherical fast winds into the GISW formalism with an application to LBVs as a class of outflows. In future papers we will attempt to apply our results to individual

LBVs in an attempt to make detailed contact with observational results.

The organization of the paper is as follows: In section II we describe the numerical method and initial conditions used in our simulations. In Section III we present and discuss the results of our simulations. In section IV we present our conclusions along with a discussion of some issues raised by the simulations.

## 2. Computational Methods and Initial Conditions

The gasdynamic interactions we wish to study are governed by the Euler equations with a ‘sink’ term in the energy equation due to radiation losses.

$$\frac{\partial \rho}{\partial t} + \nabla \cdot \rho \mathbf{u} = 0, \quad (1)$$

$$\frac{\partial \rho \mathbf{u}}{\partial t} + \nabla \cdot \rho \mathbf{u} \mathbf{u} = 0, \quad (2)$$

$$\frac{\partial E}{\partial t} + \nabla \cdot \mathbf{u}(E + p) = -\frac{\rho^2}{\bar{m}} \Lambda(T), \quad (3)$$

where

$$E = \frac{1}{2} \rho |\mathbf{u}|^2 + \frac{1}{(\gamma - 1)} p, \quad (4)$$

and

$$p = \rho \frac{k}{\bar{m}} T \quad (5)$$

In the above equations  $\bar{m}$  is the mean mass per particle and  $\gamma$  is the ratio of specific heats which we take to be  $\gamma = 5/3$ .

We have carried out our study using the Total Variation Diminishing (TVD) method of Harten (1983) as implemented by Ryu *et al* (1995). The TVD code is an explicit method for solving the Euler equations which achieves second order accuracy by finding approximate solutions to the Riemann problem at grid boundaries while remaining non-oscillatory at shocks through the application of a lower order monotone scheme. For this study we used the code configured in cylindrical coordinates  $(r, z)$ .

The cooling term  $\Lambda(T)$  was calculated via look-up tables for  $\Lambda(T)$  taken from the coronal cooling curve of Dalgarno & McCray 1972. In the TVD code the cooling is applied in between hydro timesteps via an integration of the thermal energy( $E_t$ ) equation,

$$\frac{dE_t}{dt} = -\dot{E}_t = -\frac{\rho^2}{\bar{m}} \Lambda(T). \quad (6)$$

If the cooling time scale becomes smaller than the dynamical time scale, the cooling term becomes a "stiff" source term. There are several ways to handle stiff source terms (see, *e.g.*, LeVeque 1997). First, the cooling time scale as well as the Courant condition is considered to determine the timestep. Then, in some situations, the timestep is governed by the cooling time scale and becomes uncomfortably too small. Second, Strang's operator splitting is employed, where the cooling is computed by multiple steps with its own timestep during one hydrodynamic timestep. Third, the solution takes the form

$$E_t^{n+1} = E_t^n \exp\left(-\frac{\dot{E}_t^n}{E_t^n} \Delta t\right), \quad (7)$$

where the superscript  $n$  refers to the time index. In this method, the cooling is computed in a single step. It produces good results even though the cooling time scale is smaller than the dynamical time scale. When cooling is small, the solution approaches the conventional form

$$E_t^{n+1} = E_t^n - \dot{E}_t^n \Delta t. \quad (8)$$

The third method has been used in our simulations. The term in the exponential can be expressed as  $\Delta t / \Delta t_c$  where  $\Delta t_c$  is the local cooling timestep of the gas  $\Delta t_c = \dot{E}_t^n / E_t^n$ . Although the method works well for small cooling timestep, for safety we have used

$$\Delta t = \min[\Delta t_h, 1.5\Delta t_c], \quad (9)$$

where  $\Delta t_h$  is the dynamical timestep set by the Courant Condition.

Care must be taken in the application of cooling near contact discontinuities (CDs) where in typical wind blown bubble temperatures and densities can vary by more than an order of

magnitude going from low to high values of density and high to low values of temperature. In simulations with less than perfect resolution the CD will be smeared out across a number of cells. In these intermediate zones which have both high density and high temperature the cooling term can be anomalously large. This leads to the removal of prodigious amounts of energy from the system at just a few zones. To avoid these problems we have tracked the CD by following the advection of a passive tracer  $\psi$  via Eq. (1), *i.e.*

$$\frac{\partial\psi}{\partial t} + \nabla \cdot \psi \mathbf{u} = 0. \quad (10)$$

This equation has been solved with the TVD code. Using this tracer we can distinguish between shocks and CDs. If the fast stellar wind has  $\psi = 1$  and the slow material initially filling the grid has  $\psi = 0$  then a CD can always be marked as a location with  $0.1 < \psi < 0.9$ . When a CD is encountered we replace the anomalous cooling value with one obtained from an average of the 8 nearest neighbor cells which do not contain the CD. Tests of the code show that this formalism allows us to reproduce analytically derived shock speeds (Koo & McKee 1992) for spherical radiative bubbles in a variety of power-law,  $\rho \propto r^k$ , environments.

Our numerical experiments are designed to study the evolution of wind-blown bubbles driven by aspherical fast winds. The environment is always assumed to be characteristic of a previously deposited spherically symmetric “pre-outburst” wind which we denote as wind 0 with mass loss rate  $\dot{M}_0$  and velocity  $V_0$ . Thus  $\rho_0 = \dot{M}_0/4\pi r^2 V_0$ . For the driving “fast” or “outburst” wind, which we denote as wind 1, we need a formalism for setting the latitudinal ( $\theta$ ) variations in the wind properties, *i.e.*  $\dot{M}_1 = \dot{M}_1(\theta)$  and  $V_1 = V_1(\theta)$ . We note that since we wish to drive prolate bipolar bubbles we always assume that the velocity at the poles is larger than at the equator

We have chosen to explore 3 models for the pole to equator variation in wind parameters. Each model is based on the assumption of a different quantity remaining constant across the face of the star. Our three models are:

1. Constant Momentum Input

- $\dot{\Pi} = \dot{M}_1 V_1 = Const$



2. Constant Energy Input

- $\dot{E} = \frac{1}{2}\dot{M}_1 V_1^2 = Const$

3. Constant density

- $\rho_1 = Const$

If we choose our fiducial values for the density and velocity at the equator  $(\rho_{1e}, V_{1e})$ , then the variation of these quantities can be expressed as  $\rho_1(\theta) = \rho_{1e}g(\theta)$ , and  $V_1(\theta) = V_{1e}f(\theta)$ . We can then write  $g(\theta) \propto f(\theta)^n$ . For case 1 where  $\dot{\Pi} = Const = \dot{\Pi}_e$ , we have

$$\dot{\Pi} = \dot{M}_1(\theta)V_1(\theta) = (4\pi R_*^2 \rho_1(\theta)V_1(\theta))V_1(\theta) = (4\pi R_*^2 \rho_{1e}V_{1e})V_{1e}. \quad (11)$$

Thus

$$g(\theta) = \frac{1}{f(\theta)^2}. \quad (12)$$

For case 1  $n = -2$ . Similarly, for cases 2 and 3 one finds  $n = -3$  and 0 respectively.

For  $f(\theta)$  we have chosen an ad hoc function which produces a smooth variation in  $V_1$  and  $\rho_1$  from equator to pole. Written in terms of velocity we have

$$V_1(\theta) = V_{1e} \left[ 1 - A \frac{\exp(-2B \cos(\theta)^2) - 1}{\exp(-2B) - 1} \right]^{-1}, \quad (13)$$

where constant  $B$  determines the shape of the equator to pole variability. The constant  $A$  is related to the magnitude of the contrast  $A = 1 - q_v$ . Note in what follows we shall write  $q_x = X_e/X_p$  and  $X$  is either the velocity or the density. Note that  $V_p = V_e/(1 - A)$  so  $V_p = V_e/q_v$ . We take  $A < 1$ , so that together with Eq. (12) we have  $q_v = V_e/V_p < 1$  and  $q_\rho = \rho_e/\rho_p > 1$ . These relations express our assumptions about the velocity variation across the face of the star and its consequences for the density distribution given our different models. In Fig. 1 we show a plot of the fast wind  $V(\theta)$  and  $\rho(\theta)$  for each of our three cases.

Using the formalism described above we have carried out three sets of numerical experiments varying the assumptions about the mass loss rates in the successive winds between each set.

Within the first two sets we performed a triplet of simulations with the  $\theta$  dependence of  $\dot{M}_1$  and  $V_1$  corresponding to the three cases discussed above. In set 1 we examined the interaction between two winds of with equal mass loss rates. These simulations are performed to give us a baseline on the gas-dynamic flow pattern. In the second set of experiments we examined the interaction between two winds where the previously ejected “slow” pre-outburst wind ( $\dot{M}_0$ ) had a lower mass loss rate than the outburst wind. We examine this case because stellar evolution models show the mass loss rate increases during an LBV eruption (Langer *et al.* 1994). In the third set of experiments we examined the interaction of *three* winds where  $\dot{M}_0 = \dot{M}_2 < \dot{M}_1$  and  $V_0 < V_1 < V_2$ . In these simulations only the outburst wind is considered to be aspherical. We examine this case to explore the effect of the post outburst wind on the nebular morphology. We note that the velocity difference between pre and post outburst winds may not be physically realized. As we shall discuss in a section 3.3 this assumption should not effect our results significantly. The initial conditions for each of our 9 simulations including the index  $n$  of the density function (*i.e.* Eq. 12) are given in table 1.

The mass loss rates use in our simulations range from  $\dot{M} = 10^{-6} M_{\odot} \text{ yr}^{-1}$  to  $\dot{M} = 10^{-4} M_{\odot} \text{ yr}^{-1}$ . Our wind velocities vary between  $100 \text{ km s}^{-1}$  and  $1400 \text{ km s}^{-1}$ . These values are representative of what is observed in LBVs (Leitherer *et al.* 1994) with the highest velocities seen in  $\eta$  Car (Ebbets *et al.* 1997). We note that in giant outbursts the mass loss rates may increase by an order of magnitude or more over what is used in this study (Humphreys & Davidson 1994). We have chosen not to use larger values of the mass loss rate based on the short cooling timescales which occur in high density winds. Short timescales would force us to use lower resolution simulations given constrains on computational time. We decided that achieving higher resolution ( $256 \times 256$ ) was a more important goal since, based on our results, we will be able to anticipate the enhanced cooling effects of higher mass loss rates. We note that the simulations were all run until the outer shock ran off the grid. Thus the timescale for each simulation is essentially the dynamical age of the bubble for  $R \approx 5 \times 10^{17} \text{ cm}$ .

### 3. Results

#### 3.1. 2 Wind Models with Equal $\dot{M}$

Fig. 2 shows  $\rho$ ,  $T$ ,  $\vec{V}$ , and  $P$  for run A after  $t = 800$  yrs of evolution. Run A has an outburst stellar wind whose momentum flux  $\dot{\Pi}$  is constant across the face of the star. A number of features of the simulation are noteworthy but it is first worthwhile to identify the main features of the wind blown bubble. The density map shows a bright rim which corresponds to the shell of swept-up pre-outburst wind material. It is important to distinguish the composition of the material in the shell (*i.e.* which wind it originates from) since its high density will make it most luminous and, therefore, the defining feature in a real nebula. Fig. 2 shows that the shell develops significant asphericity due to the aspherical driving force of the outburst wind. For later comparison we introduce a quantity we call the ellipticity defined as the ratio of the distance from the star to the outer shock in the equator and the pole,  $e = R_e/R_p$ .  $e \approx 0.68$  in this simulation. Notice also that the bubble has developed a “waist” which is the observational signature of a bipolar rather than an elliptical configuration. The density map for Run A is also shown in Fig. 4 with the appropriate reflections to create a slice of the full bubble.

Detailed inspection of the  $\rho$  and  $T$  maps show that the shell is thin and cold ( $T \approx 10^4 K$ ) at all latitudes. The narrowness of the shell is due to the enhanced compression which accompanies radiative losses behind the outer shock. The role of cooling is important and is determined by the relation between the age of the bubble and the cooling timescale. Given a shock speed  $V_s$  and a preshock density of  $\rho_{pre}$  the cooling timescale can be defined as  $t_c = CV_s^3/\rho_{pre}$  where  $C = 6 \times 10^{-35} g cm^{-6} s^4$  (Kahn 1976). The outer shock speed in this simulation is on the order of 200 km/s. Taking  $\rho_{pre}$  from the mass conservation in the pre-outburst wind gives  $t_c = 150y$  which is short compared to the age of the bubble in Fig. 2.

The situation is quite different behind the “reverse ” or “inner” shock. At low latitudes the speed of the outburst wind is relatively small (150 km/s) and the density is relatively high producing a short cooling time. The reverse situation occurs at the poles where the high wind

velocity (750 km/s) and low pre-shock density yield cooling times which are of the same order or longer than the age of the bubble. This produces a cap of high temperature gas at the poles. High thermal pressure enhances the preferential expansion at the poles which leads to a bipolar bubble. We note however that even when the cooling at the poles is strong enough to drain away all shock thermalized energy the bubble which is produced is still bipolar.

The density maps for run B and C are presented in Fig. 4. Run B corresponds to the case where the energy input in the wind,  $\dot{E}_1$ , is constant across the face of the star. The morphology of the bubble in run B is similar to that in run A. The principle difference being the aspect ratio of the bubble. This can be attributed to the differing latitudinal density profiles for the two runs. From Eq. (12) the  $\dot{I}_1 = Const$  simulation (run A) has  $\rho \propto f(\theta)^{-2}$ . The  $\dot{E}_1 = Const$  simulation (run B) yields  $\rho \propto f(\theta)^{-3}$ . For run C the density in the wind is constant and is set by the value in the equator where  $V_1(\theta)$  has its minimum. Since  $\rho \propto \dot{M}/V$  via the continuity equation the outburst wind density in run C is almost as high as that in the pre-outburst wind. This produces a strong ram pressure flux ratio between the two flows. The initial shape of the outburst wind is strongly imprinted on the developing bubble. Thus run C produces most bipolar shell of all three simulations examined in this first set of experiments.

The results presented above show that bipolar bubbles can form when driven by an aspherical fast wind. The differences between the three models also demonstrates that the degree of bipolarity does depend on relative densities between the aspherical fast (outburst) wind and the spherically symmetric slow pre-outburst wind.

### 3.2. 2 Wind Models with $\dot{M}_1 > \dot{M}_0$

As Langer *et al.* 1994 have demonstrated with stellar evolution codes, the LBV outburst phase is likely to involve an increase in mass loss over the pre-outburst wind. Thus we have the case of a “heavy” wind expanding into a light one. In this situation the pre-existing circumstellar material can not constrain the outflow. The wind will not be significantly decelerated by the environment

until the swept-up mass is comparable to the mass ejected by the wind. Given that the outburst mass loss rate can be an order of magnitude or more greater than the pre-outburst value, the outburst wind can expand almost ballistically for some time. If, in addition, the outburst wind is aspherical, then the bubble which is created will retain much of the asphericity imprinted on the wind at the stellar surface. In this scenario we expect that one gets out something similar to what is put in via the initial density and velocity distributions for the outburst wind. To test this expectation we have run a second set of experiments consisting of three simulations. Runs D, E and F have  $\dot{\Pi}_1$ ,  $\dot{E}_1$  and  $\rho_1$  held constant respectively just as in the simulations described in the last section. In these simulations however  $\dot{M}_1 = 100\dot{M}_0$ . Note that for the sake of consistency with the previous experiments we have used the same velocity in the pre-outburst wind as was used in runs A through C. The results of Langer *et al.* 1994 show that the velocity in the pre-outburst wind should be higher than that in the outburst wind. We do not believe such a difference will produce a profound change in our results. A high velocity pre-outburst wind will interact with the ISM producing shocked gas which backflows to the boundary of the pre-outburst wind. Such a high pressure region will still yield an isotropic force opposing the expansion of the outburst wind. Thus while the details of the flow may change, the global properties most likely will not be affected.

Fig. 3. shows a snapshot of the evolution of run D after  $t = 240yrs$ . As expected the bubble formed appears strongly bipolar with an ellipticity of  $e = 0.4$ . While such a result was expected from intuitive arguments a ballistic expansion model does not tell the whole story. Note first that run D has reached the same size ( $R_e = 5.1 \times 10^{17}$  cm) as run A in about a third of the time giving an expansion velocity along the pole of  $V_s \approx 660$  km/s. This is less than the outburst wind velocity at the poles  $V_1 = 750$  km/s. Ambient material which passes through shock can be expected to reach high temperatures of the order of  $T \sim 10^7$  K where cooling is relatively ineffective. The temperature map clearly shows high  $T$  gas at the top of the bubble. Consideration of the passive tracer shows that this is ambient material which has been accelerated. The temperature map also shows lower temperature gas at smaller radii. This is outburst wind material which has passed through the inner shock which can be seen at  $R_e = 4.2 \times 10^{17}$  cm. Consideration of the position

of the shock compared with the position expected for ballistic winds yields a inner shock velocity of  $V_s \approx 200 \text{ km s}^{-1}$ , consistent with the temperature in this region (measured to  $T \approx 10^6 \text{ K}$ ). The presence of this shock indicates that the outburst wind gas parcels are being decelerated by the swept-up ambient material. This deceleration occurs because of the low outburst wind density along the poles as can see from the density map. Recall that we are using equator to pole velocity contrast of  $q_v = 1/5$ . This produces a equator to pole density contrast of  $q_\rho = 1/q_v^2 = 25$ .

Runs E and F show similar morphologies though the  $\rho = \text{Const}$  case again produces the most bipolar configuration. We note that for Run E and F  $e = 0.42$  and  $0.36$  respectively. In Fig. 4 we present  $\log_{10} \rho$  maps for runs A through F. In each map we have reflected the computational space about the symmetry axis ( $r = 0$ ) and symmetry plane ( $z = 0$ ) to show the full bubble cross section and facilitate comparison. In spite of the differences between the runs, Fig. 4 demonstrates the principle conclusion of our first two sets of experiments: an *aspherical stellar wind can drive an aspherical bubble*.

### 3.3. 3 Wind Models

In this section we present the results of our final set of numerical experiments where we take a step closer to reality by invoking three wind models. In runs G, H, and I we have performed simulations with conditions in the pre-outburst and outburst winds similar to run D. In these runs however the outburst wind lasts only 30 years after which a “post-outburst” wind is driven into the grid. The characteristics of the post-outburst wind were meant to mimic the conditions currently observed in  $\eta$  Carinae in the sense that we used a relatively low mass rate and high velocity for the wind, *i.e.*  $\dot{M}_2 < \dot{M}_1$  and  $V_2 > V_1$ . Recall that in the simulations of GLM it was the fast post-outburst wind which was responsible for driving the bipolar  $\eta$  Car bubble. In these simulations we are interested in what effect this post-outburst wind will have on a bipolar bubble created by a previously ejected dense aspherical wind. We note that the post-outburst wind in all of these simulations is spherical and will produce an isotropic driving force.

We have run three simulations each of which utilized the  $\dot{M} = Const$  formalism. In these simulations it was  $q_v$ , the equator to pole velocity contrast in the outburst wind, which was varied. The purpose of this strategy was to understand how the additional driving force provided by the post-outburst wind would effect bubbles with different degrees of bipolarity.

Fig. 5 shows a snapshot of the evolution of run H after  $t = 250yrs$ . This simulation has an outburst wind with  $q_v = 1/7$  and  $q_\rho = 49$ . Unlike the last set of experiments here the gas ejected during the outburst in these models occupies a thin shell. The reasons for this are twofold. First, the outburst had a short intrinsic lifetime (which we denote as  $t_1$ ) so its intrinsic width is  $\delta R = V_1 t_1$ . Second, the outburst material has been decelerated and compressed from the outside by the pre-outburst wind and compressed and accelerated from the inside by the action of succeeding post-outburst wind. Note that the post-outburst wind has itself been decelerated through the action of a strong inner shock. The temperature behind this shock at the poles is quite high ( $T \approx 2. \times 10^7$  K) reflecting the high initial velocity of the post-outburst wind. The inner shock has a highly aspherical configuration. The radially streaming post-outburst wind encounters this shock at oblique angles and is refracted towards the symmetry axis (Frank & Mellema 1996). This produces strong shearing flows in the region behind the inner shock which appear to give rise to instabilities in the interface separating the shocked post-outburst and outburst flows.

In Fig. 6 we present  $\log_{10} \rho$  maps for all three simulations from this set of experiments. Again it is clear that strong bipolar morphologies develop without the need for a slow-moving disk. Comparison between the simulations shows that decreasing  $q_v$  produces stronger bipolar morphologies. It is worth noting that if the expansion of the bubble were ballistic then we would expect  $e \approx q_v$  since  $R_e = V_{1e}t$  and  $R_p = V_{1p}t$ . This is not the case. Thus these bubbles show the result of significant hydrodynamic shaping. Some part of the change in the shape results from the deceleration of the outburst wind via the previously ejected material. The post-outburst wind however also contributes by accelerating the outburst wind material. As the bubble evolves this acceleration will have its greatest effect near the equator where the outburst wind has been most strongly decelerated. Thus the action of the post-outburst wind will be to drive the bubble towards

a more spherical configuration as system evolves. We note however that the post-outburst might also be aspherical. As was noted above Leitherer *et al.* 1994 have observed two components in the wind of AG Car. An strong aspherical post outburst wind would then increase the elongation of the bipolar lobes. Further observational study of the characteristics of LBV winds are warranted to determine the latitudinal density and velocity variations.

#### 4. Discussion and Conclusions

The results of our simulations demonstrate that bipolar wind blown bubbles can result purely from the action of an aspherical fast wind. In previous studies of LBV bubbles (FBD, NLCS, GLM) it has been assumed that a slow moving torus or disk of gas was a necessary precondition for the development a bipolar bubble. Our results indicate that the properties of LBV bubbles may not require such a torus to form either before (FBD, NLCS) or during (GLM) the outburst.

Our scenario has a number of attractive features. First it is both observationally and theoretically motivated. From the observational side there is already evidence that LBV winds can take on aspherical velocity and density distributions. From the theoretical side the theory of Lamers & Pauldrach 1991 have demonstrated that "bistable" winds are possible around massive hot stars. In addition, the diversity of shapes of LBV bubbles (NLCS) may be difficult to achieve with pre-existing disk models. The models presented here can recover the diversity of shapes simply by changing  $q_v$  though it is certainly true that this also begs the question of what drives the velocity contrast in the fast wind.

Currently it is unclear what form the mass distribution takes in the lobes of LBV bubbles. One critical test of the different models for LBV nebula shaping would entail comparison of latitudinal variations of mass. If the caps of a bipolar lobe have densities that are comparable to that in the lobe's flanks it would present difficulties for the slow torus models. In a bipolar bubble resulting from a spherical fast wind driving into a slow torus the caps of the bubble should be the location of the lowest density. For aspherical fast winds however high or equal density in the poles



poses no significant problem since we are then seeing a signature of the latitudinal dependence of the fast wind density (consider Runs C and F in Fig. 3). We wish to note also that Currie *et al.* 1996b and Morse *et al.* 1997 have found that the shape of  $\eta$  Car is best matched by a geometry which can be described as a "double flask" rather than an two osculating spheres. Based on comparison of published results the models presented here seem to do a better job of recovering such a shape than either FBD, NLCS or GLM.

It is noteworthy however that the scenario presented here would not produce the equatorial "skirt" seen surrounding the waist of the homunculus in  $\eta$  Car. The presence of that feature is what motivated the original application of the GISW slow torus models. Within the current formulation of the aspherical fast wind model there is not a likely means of producing such a feature. A few points are worth noting however. The equatorial skirt is not a continuous or even axisymmetric feature. Thus whatever its origin it is hard to imagine that it can be the agent which constricts a spherical fast wind and produces the bipolar bubble. In addition there are a number of "spikes" extending beyond, but connecting with the homunculus that have been reported to have velocities in excess of 1000 km/s (Meaburn *et al.* 1996). They yield dynamical timescales  $\leq t_o$  where  $t_o$  is the time since the outburst. Thus it is possible that the equatorial skirt is actually a spray of material which ejected at some point after the outburst of 1849 and which was decelerated by its passage through the dense shell of the outburst wind. The non-axisymmetric distribution of the skirt may then be a consequence of the intrinsic pattern of ejecta or of impulsive instabilities which will occur when the ejecta is driven through the outburst wind.

Regardless of the answer to this issue the results presented here show that there are two very different scenarios for the formation of LBV bubbles. Either they form via the interaction of a spherical fast wind driving into an aspherical slow wind (a slow torus) or they form from an aspherical fast wind driving into an isotropic pre-existing environment. This embarrassment of riches can be eventually be dealt with by comparing the latitudinal distributions of mass and momentum observed in real bipolar LBVs with what is predicted for the various models. Such an approach was used successfully by Masson & Chernin 1992 in evaluating different models of

molecular outflow formation in YSOs. This project is currently in progress.

We wish to thank Jon Morse, Jon Bjorkman, Tom Jones and Stan Owocki for the very useful and enlightening discussions on this topic. Support for AF was provided by NASA grant HS-01070.01-94A from the Space Telescope Science Institute, which is operated by AURA Inc under NASA contract NASA-26555. Additional support for AF came from NSF Grant AST-9702484 and the Minnesota Supercomputer Institute. Partial support for DR was provided from Seoam Scholarship Foundation.

Table 1: Initial Conditions For Runs A - H

run	$\dot{M}_0$	$V_0$	$\dot{M}_1$	$V_1$	$\dot{M}_2$	$V_2$	$q_v$	Con. Index
A	$1 \times 10^{-4}$	100	$1 \times 10^{-4}$	150	NA	NA	0.2	-2
B	$1 \times 10^{-4}$	100	$1 \times 10^{-4}$	150	NA	NA	0.2	-3
C	$1 \times 10^{-4}$	100	$1 \times 10^{-4}$	150	NA	NA	0.2	0
D	$1 \times 10^{-6}$	100	$1 \times 10^{-4}$	150	NA	NA	0.2	-2
E	$1 \times 10^{-6}$	100	$1 \times 10^{-4}$	150	NA	NA	0.2	-3
F	$1 \times 10^{-6}$	100	$1 \times 10^{-4}$	150	NA	NA	0.2	0
G	$1 \times 10^{-6}$	100	$1 \times 10^{-4}$	150	$1 \times 10^{-6}$	1400	0.3	-2
H	$1 \times 10^{-6}$	100	$1 \times 10^{-4}$	150	$1 \times 10^{-6}$	1400	0.14	-2
I	$1 \times 10^{-6}$	100	$1 \times 10^{-4}$	150	$1 \times 10^{-6}$	1400	0.1	-2

## REFERENCES

- Balick, B., 1987, AJ, 94, 671
- Bjorkman, J., & Cassinelli, J., 1992, ApJ, 409, 429
- Blondin, J., & Lundqvist, P., 1993, ApJ, 405, 337
- Currie, D., Dowling, D., Shaya, E., Hester, J., Scowen, P., Groth, E., Lynds, R., O’Neil E., 1996, AJ, 112, 1115
- Currie, D., Dowling, D., Shaya, E., Hester, 1996, in *The Role of Dust in Star Formation*, ESO Workshop, ed. H. Kauff (New York, Springer Verlag 1989)
- Dalgarno, A., & McCray, R., 1972, ARA&A, 10, 375
- Davidson, K., Ebbets, D., Weigelt, G., Humphreys, R., Hajian, A., Walborn, N., & Rosa, M., 1995, AJ, 109, 1784
- Ebbets, D., Garner, H., White, R., Davidson, K., & Walborn, N., 1993, in *Circumstellar Media in the Late Stages of Stellar Evolution*, Proc. 34th Herstmonceux Conf. (Cambridge: Cambridge Univ. Press)
- Ebbets, D., Morse, J., Davidson, K., & Walborn, N., 1997, in “Luminous Blue Variables: Massive Stars in Transition” ed A. Nota & J.G.L.M. Lamers, (ASP Conference Series, San Francisco)
- Frank, A., Balick, B., Icke, V., & Mellema, G., 1993, ApJ, 404, L25
- Frank, A., & Mellema, G., 1994, ApJ, 430 800
- Frank, A., Balick, B., & Davidson K., 1994, ApJ, 441L, 77 (FBD)
- Frank, A., Balick, B., & Livio, M., 1996, ApJ, 471, L53
- Frank, A., & Mellema, G., 1996, ApJ, 472, 684

- Garcia-segura, G., Langer, N., & Mac Low, M., 1997, in “Luminious Blue Variables: Massive Stars in Transitio” ed A. Nota & J.G.L.M. Lamers, (ASP Conference Series, San Francisco)
- Hester, J. J., Light, R. M., Westphal, J. A., Currie, D. G., & Groth, E. J., 1991, *AJ*, 102, 654
- Harten, A., 1983, *J. Comp. Phys*, 49, 357
- Humphreys, R., & Davidson, K., 1994, *PASP*, 106, 1025
- Ignace, R., Cassinelli, J., & Bjorkman, J., 1996, *ApJ*, 459, 671
- Kahn, F. D., 1983 in “IAU Symposium 103: Planetary Nebulae” ed D. Flower (Reidel, Dordrecht)
- Kwok, S.; Purton, C. et al. 1978, *ApJ* 219, L125
- Kwok, S., 1982, *ApJ* 258, 280
- Lamers, H., & Pauldrach, A., 1991, *A&A*, 244L, 5
- Langer, N., Hamann, W.-R., Lennon, M., Najarro, F., Pauldrach, A., & Puls, J., 1994, *A&A*, 290, 819
- Leitherer, C., Allen, R., Altner, B., Daminieli, A., Drissen, L., Idiart, T., Lupie, O., Nota, A., Schmutz, W., & Shore, S., 1994, *ApJ*, 428, 292
- Leitherer, C., 1997, in “Luminious Blue Variables: Massive Stars in Transitio” ed A. Nota & J.G.L.M. Lamers, (ASP Conference Series, San Francisco)
- Kahn, F., 1976, *Å*, 50, 145
- Koo, B., & McKee, C. F., 1992, *ApJ*, 388, 103
- Manchado, A., Guerrero, M., Stanghelli, L., & Serra-Ricart, M., 1996 The IAC Catalog of Northern Galactic PNe, (IAC, La Laguna)
- Masson, C. R. & Chernin, L. M. 1992, *ApJ*, 387, L47

- Meaburn, J., Boumis, P., Walsh, J. R., Steffan, W., Holloway, A. J., Williams, R. J. R., & Bryce, M., MNRAS, in press
- Mellema, G., Eulderink, F., & Icke, V., 1991, A&A, 252, 718.
- Mellema, G., & Frank, A., 1995, MNRAS, 273, 401
- LeVeque, R. J., 1997, in Computational Methods in Astrophysical Fluid Flows, 27th Saas-Fee Advanced Course Lecture Notes, to be published by Springer Verlag.
- Morse, J., Davidson, K., Ebbets, M., & Walborn, N, Balick, B., Frank, A., & Bally, J., 1997, AJ, submitted
- Nota, A., Livio, M., Clampin, M., & Schulte-ladbeck, R., 1995, ApJ, 448, 788 (NLCS)
- Nota, A., Clampin, M., Pasquali, A., Pollacco, D., Scuderi, S., & Livio, M., 1996, ApJ, 473, 946
- Owocki, S., Cranmer, S., & Gayley, K. G., 1996 ApJ, 472L, 115
- Pauldrach, W.A., & Puls, J., 1990, A&A, 237, 409
- Ryu, D., Brown, G. L., Ostriker, J. P., Loeb, A., ApJ, 452, 364
- Weis, K., Duschl, W., Bomans, D., Chu, Y.-H., & Joner, M., 1996, A&A, in press

## FIGURE CAPTIONS

**Fig. 1** Initial conditions for aspherical fast stellar wind. The variation of stellar wind velocity and density with latitude are shown for a model with  $A = 0.1$  and  $B = 2$ . Note the equator is at  $\theta = 90^\circ$ . The velocity and density at the equator are set to 1. The density plot shows the three different cases considered in text. Solid line: momentum input  $\dot{\Pi} = \text{const}$  across face of star. Dashed line: energy input  $\dot{E} = \text{const}$ . Dashed-dot line: density  $\rho = \text{const}$ .

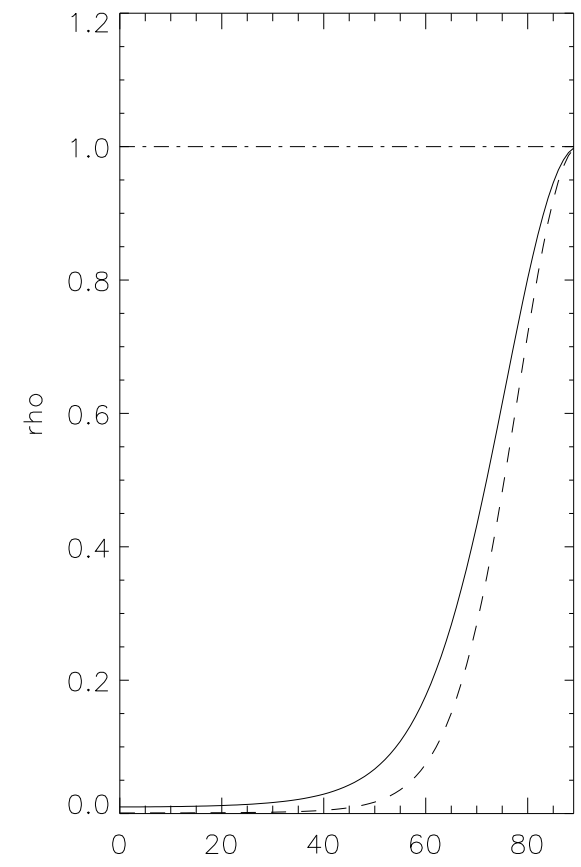
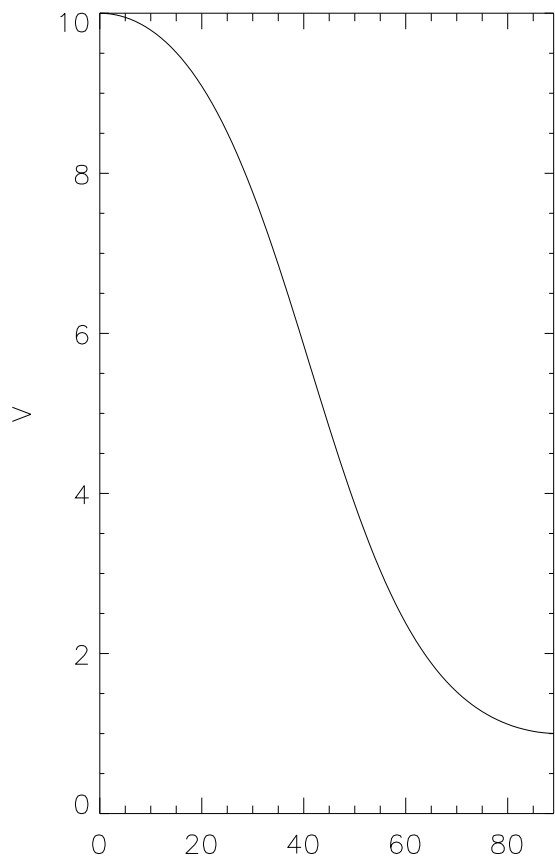
**Fig. 2** Run A after 800yrs. Shown are greyscale maps of  $\log_{10}$  number density, temperature, velocity (with vectors superposed), and pressure. Note that dark scales correspond to high values of the variables. The range of variables are as follows:  
 $.5 < \log_{10}(n/cm^{-3}) < 3.7$ ,  $3.9 < \log_{10}(T/K) < 6.8$ ,  $6.1 < \log_{10}(V/cm s^{-1}) < 7.8$ , and  
 $-11.3 < \log_{10}(P/dynes\ cm^{-2}) < -7.8$

**Fig. 3** Run D after 240yrs. The maps and parameter ranges are the same as in Fig. 2

**Fig. 4**  $\log_{10}$  grayscale density maps of runs A through F. Top Left: Run A. Top Center: Run B. Top Right: Run C. Bottom Left: Run D. Bottom Center: Run E. Bottom Right: Run F. Note that here that dark scales correspond to low values of the variables. Runs A and B are shown at  $t \sim 800yrs$ . Runs C through F are shown at  $t \sim 250yrs$ . Each image is  $1.2 \times 10^{18}$  cm square.

**Fig. 5** Run G after 250yrs. Shown are greyscale maps of  $\log_{10}$  number density, temperature, velocity (with vectors superposed), and pressure. Note that dark scales correspond to high values of the variables. The range of variables are as follows:  
 $.5 < \log_{10}(n/cm^{-3}) < 3.1$ ,  $3.9 < \log_{10}(T/K) < 7.5$ ,  $6.5 < \log_{10}(V/cm\ s^{-1}) < 8.1$ , and  
 $-11.3 < \log_{10}(P/dynes\ cm^{-2}) < -7.7$

**Fig. 6**  $\log_{10}$  grayscale density maps of runs G through I. Left: Run G. Center: Run H. Right: Run I. Note that here that dark scales correspond to low values of the variables. Each image is  $1.2 \times 10^{18}$  cm square.



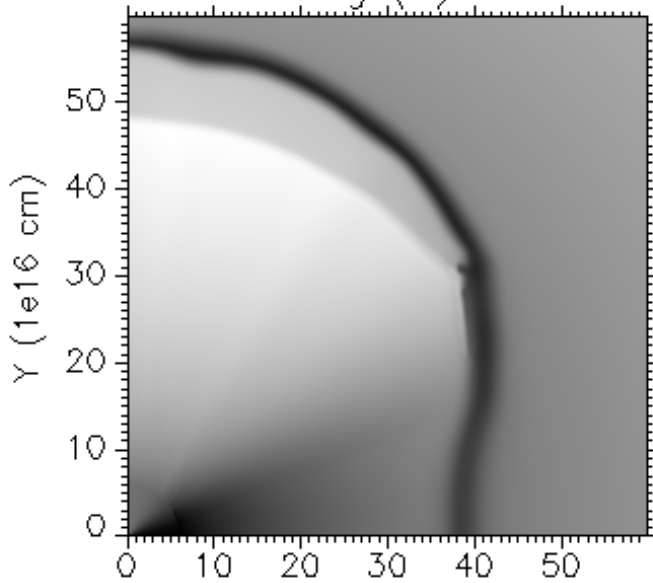


# CaseA.0926.0020

Time = 802

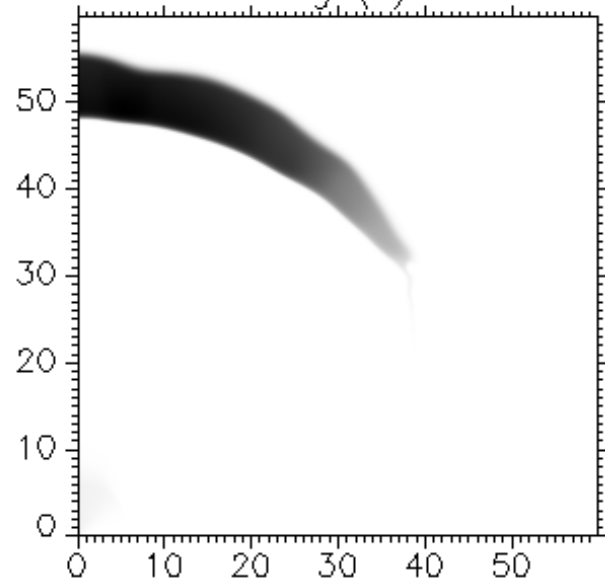
$$\begin{aligned} < \text{Log} (N) < 3.7 \\ 6.1 < \text{Log} (V) < 7.8 \end{aligned}$$

Log (N)

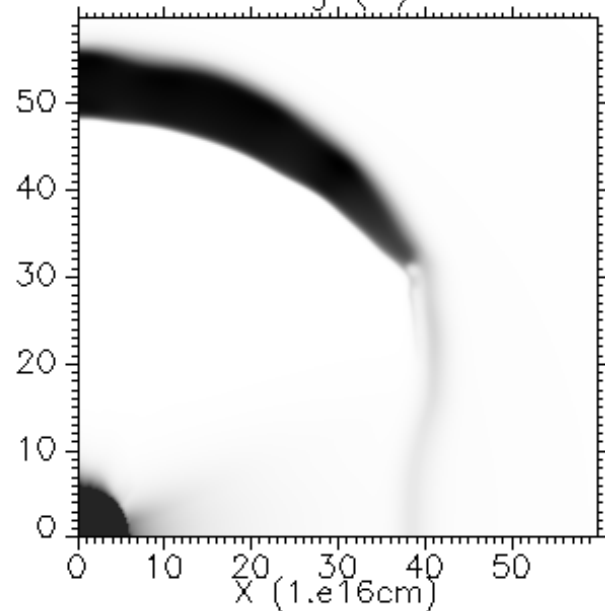
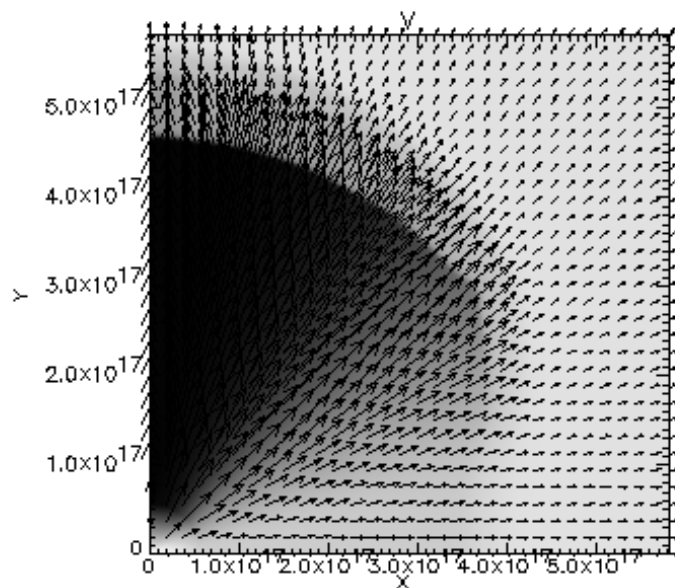


$$\begin{aligned} 3.9 < \text{Log} (T) < 6.8 \\ -11.3 < \text{Log} (P) < -7.8 \end{aligned}$$

Log (T)



Log (P)



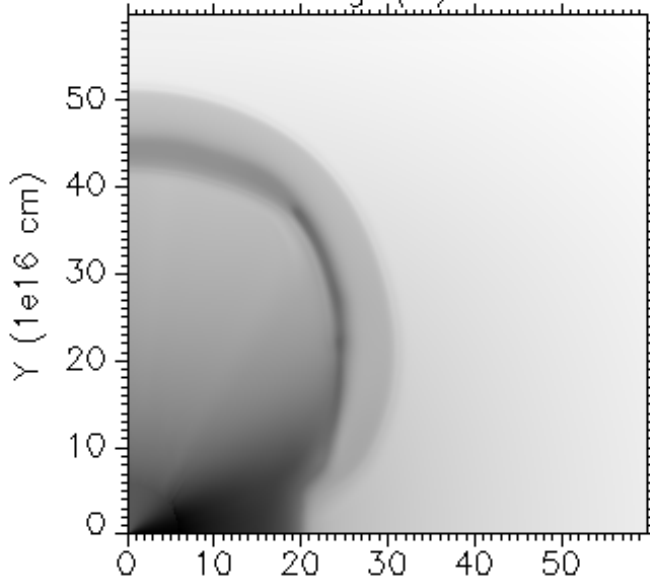
# CaseD.0926.0006

Time =240

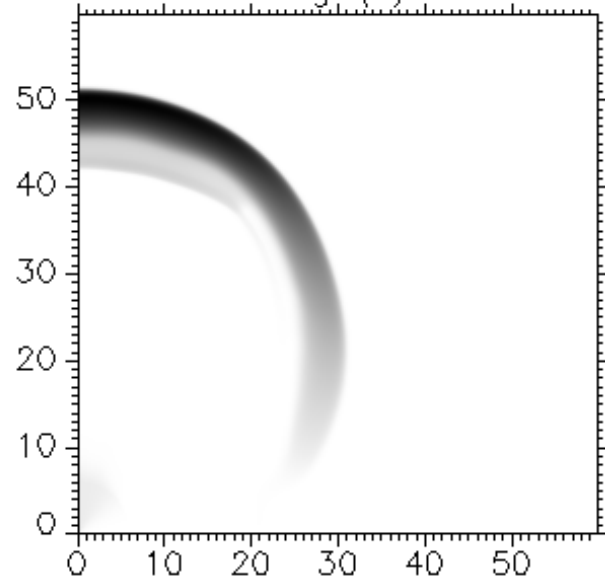
$$\begin{aligned} - < \text{Log} (N) < 3.7 \\ 6.1 < \text{Log} (V) < 7.8 \end{aligned}$$

$$\begin{aligned} 3.9 < \text{Log} (T) < 6.7 \\ -12.3 < \text{Log} (P) < -7.9 \end{aligned}$$

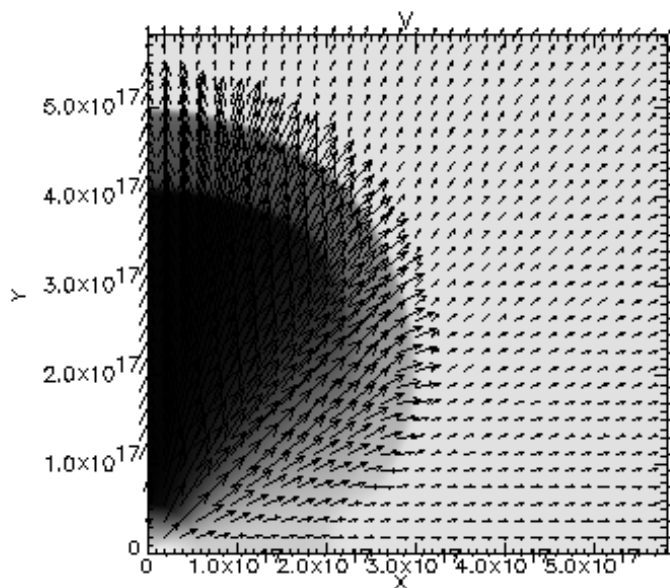
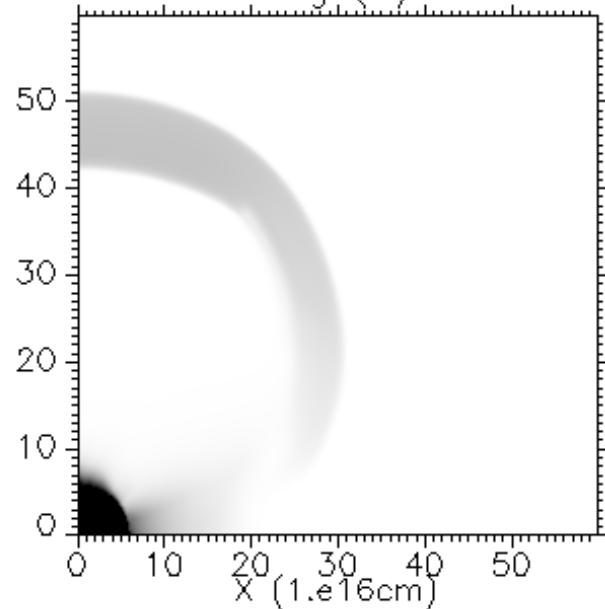
Log (N)

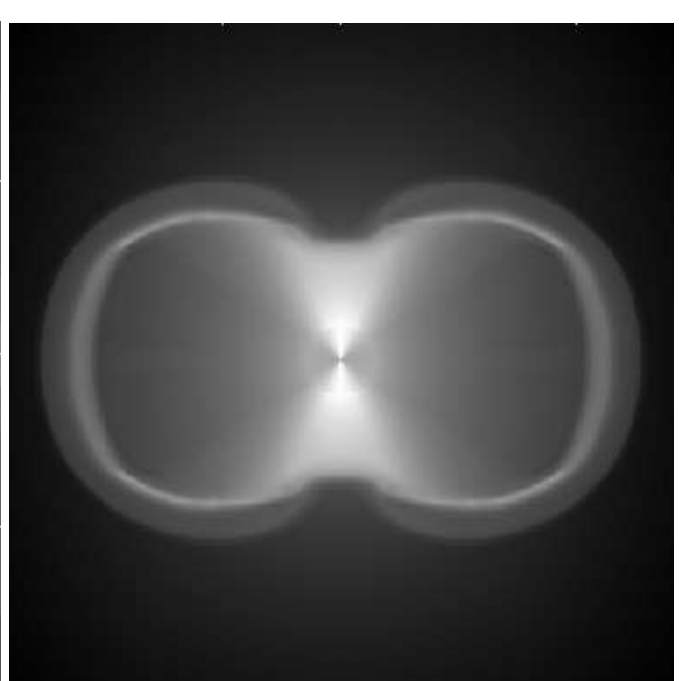
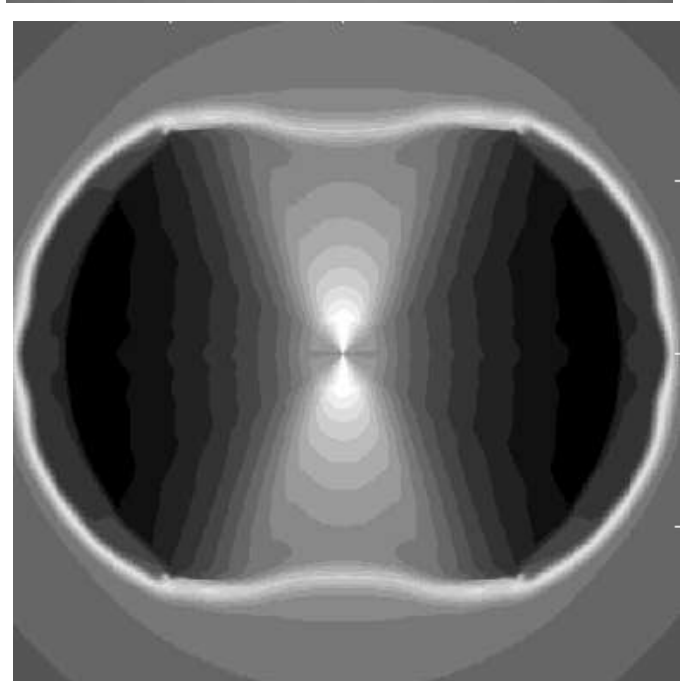
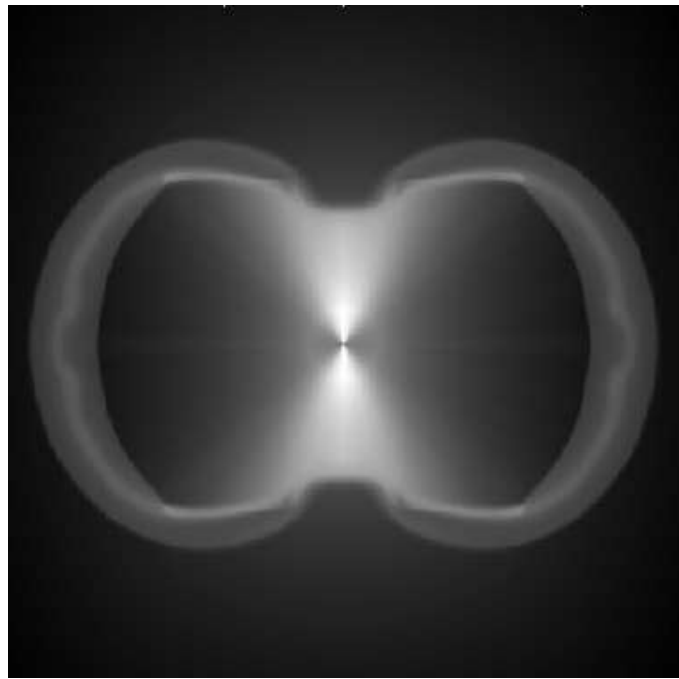
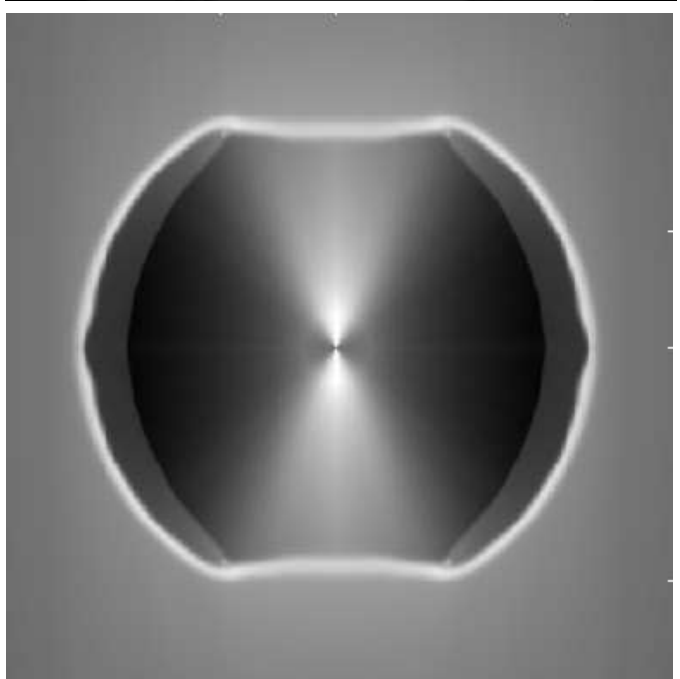
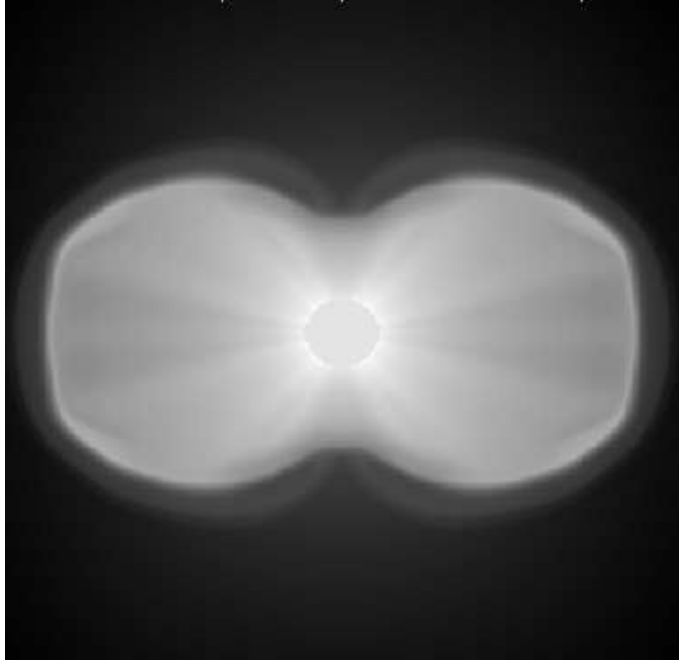
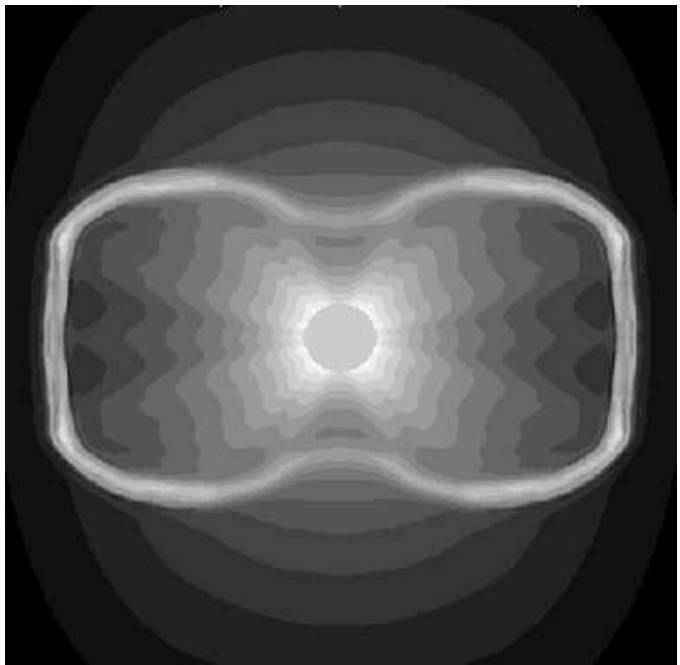


Log (T)



Log (P)





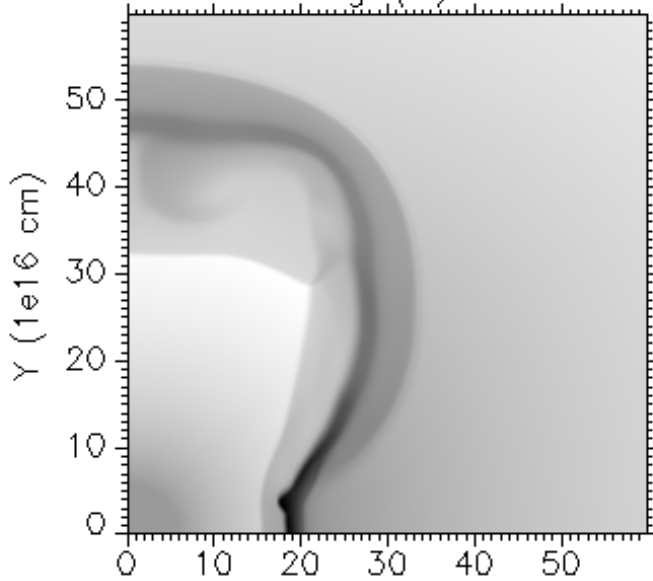
# CaseG.0926.0025

Time = 250

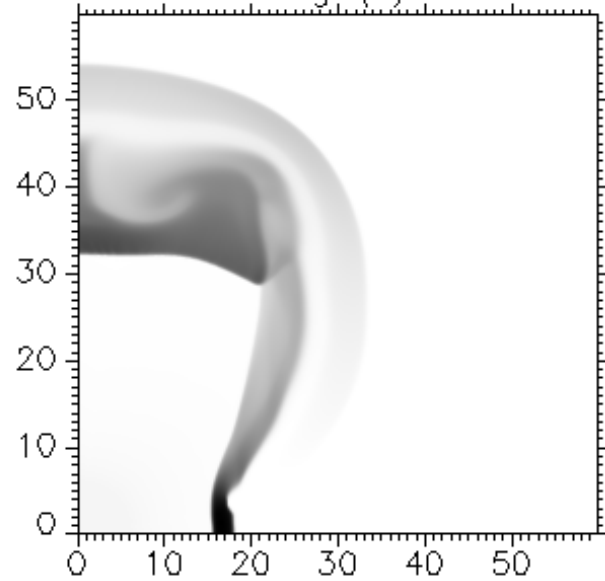
$$\begin{aligned} - < \text{Log} (N) < 3.1 \\ 6.5 < \text{Log} (V) < 8.1 \end{aligned}$$

$$\begin{aligned} -1. < \text{Log} (T) < 7.5 \\ -17.5 < \text{Log} (P) < -7.7 \end{aligned}$$

Log (N)



Log (T)



Log (P)

